PRE-HEATED SUBSTRATE EFFECTS ON MELT-MEDIATED LASER CRYSTALLIZATION OF NITI THIN FILMS

Paper (M703)

Andrew J. Birnbaum[1], Ui-Jin Chung[2], Xu Huang[3], Ainissa G. Ramirez[3], James S. Im[2], Y. Lawrence Yao[1]
[1] Mechanical Engineering Department, Columbia University, New York, NY, 10027, USA
[2] Program in Materials Science, Department of Applied Physics and Applied Mathematics, Columbia University, New York, NY, 10027, USA
[3] Mechanical Engineering Department, Yale University, New Haven, CT, 06511, USA

Abstract

Amorphous sputter-deposited NiTi thin films were subjected to pulsed, melt-mediated laser crystallization techniques to engineer their microstructure. The effects of laser processing of pre-heated films are examined. Laser processing of films at an elevated temperature has a significant effect on the rate with which solidification occurs and therefore may be used as an added parameter to control the resulting microstructure. It is seen that the temperature at which processing is carried out has significant implications for the resulting phase and microstructure, and therefore mechanical properties. Furthermore, the microstructural effects of varying incident laser energy density are examined via atomic force microscopy (AFM), scanning electron microscopy (SEM) and x-ray diffraction (XRD), and mechanical/shape memory properties are characterized via nanoindentation.

Introduction

Pulsed, melt mediated laser crystallization techniques have been studied extensively for a range of material classes including semiconductors, elements and metal alloys [1-3]. The process provides a flexible means for spatial control over crystalline/amorphous regions as well as a high degree of control over the resulting microstructure itself. By varying the incident laser energy density and patterned geometries, grain size and shape as well as texture may be specifically tailored toward a range of applications. Silicon thin films have been successfully processed in this manner for the production of thin film transistors (TFT's) for use in active matrix displays (e.g. LCD and OLED). These applications also rely on the ability of the process for controlling the density of microstructural defects (e.g. high-angle grain boundaries) which have significant effects on device performance[4]. Spaepen, Turnbull and Lin [5-7] have used the pulsed melt mediated process to produce and study the behaviour of thin film metallic glasses and thin film metallic alloys. This process is well suited toward this end owing to exceedingly high quench rates [6]. Interest in processing elemental metals has also increased as a means for producing and tailoring microstructures for interconnects in IC circuitry [8].

Pulsed, melt-mediated laser crystallization techniques have yet to be utilized in processing thin film shape memory alloys and hold great potential for control over the resulting structure. Although shape memory alloys' (SMA's) non-conventional properties have been studied extensively over the last four decades, their actual implementation has been limited due to several complicating factors. A main impediment to application, particularly for thermally-induced macro-scale actuation applications is poor dynamic response stemming from long heat dissipation times. Recently, thin film shape memory structures have received increasing attention for micro-scale actuation as they do not suffer from this limitation due to their exceedingly low thermal mass. In addition to the shape memory effect, significant attention has also been devoted to exploiting the superelastic effect. In particular, applications in improving the wear resistance of NiTi surfaces have received increasing amounts of interest [9-11].

The vast majority of this work has been limited to thin films whose shape memory properties are homogenous throughout the film. Ishida et. al. [12-14] conducted a series of in depth investigations on the effects of furnace, solid phase crystallization parameters (i.e. annealing temperature and dwell time) on the resulting shape memory properties of NiTi sputtered thin films, while Gil [15] examined the effect of grain size on martensitic phase transformation temperatures. Lee and Ramirez [16, 17] have conducted a series of investigations into the kinetics of the solid phase crystallization process via *in situ* TEM observations. A wide variety of proposed SMA-based actuation devices may be found in [18-21], again, all relying on homogenous shape memory properties.

Several investigations on the use of laser annealing in order to control the spatial extents of crystalline

regions have been conducted, although they have all been restricted to CW, solid phase processing. Bellouard et. al. [22,23] used a near IR CW laser to selectively solid-phase crystallize a sputter-deposited NiTi thin film for the purposes of fabricating a micro-gripper whose only active component was the crystallized portion of the device. He et. al. [24] investigated the use of a CW CO_2 laser to selectively anneal a NiTi thin film via solid-phase crystallization as well.

This work proposes the use of pulsed, melt-mediated laser crystallization techniques to control the spatial distribution of crystalline zones within an amorphous or pre-crystallized matrix. This process provides not only spatial control over the shape memory response, but through proper use of operational parameters, has the potential for tailoring the shape memory response itself, i.e. phase transformation temperature, transformation strain, recovery stress etc. The use of a melt-mediated process also provides several advantages over homogenous furnace annealing as well as CW, solid phase techniques. These include increased efficiency for large scale fabrication due to single shot batch processing capabilities (i.e. no rastering), increased control over the resulting microstructure, and features with sharp boundaries due to low pulse duration to thermal diffusivity time scales. Crystallization rates for the pulsed process (~nanosecond pulse durations) also far exceed those of CW processing whose scan speeds are on the order of 3-5mm/s and furnace annealing times ranging from tens of seconds to several hours. The pulsed process is also advantageous as it may be performed on device films *in situ* in fairly close proximity to other possibly thermally sensitive components.

Experimental Setup

NiTi films were deposited by simultaneous co-sputtering from an alloyed NiTi target and pure titanium target at powers of 302 and 50 watts respectively for 300 seconds at an argon pressure of 3 mTorr resulting in films 200nm in thickness. The films were deposited on a 1μm ultra-low residual stress silicon nitride (Si_3N_4) barrier layer that had been deposited on a [100] silicon wafer via low pressure chemical vapour deposition (LPCVD). The deposition was performed at room temperature, and thus resulted in an amorphous film as confirmed by x-ray diffraction (not shown). Furthermore, the film composition as Ni-52.4 at.% was obtained via a calibrated electron microprobe.

Films were single shot, pulse irradiated by a 308 nm wavelength, XeCl excimer laser with 30 ns pulse duration over a wide range of incident laser energy densities. Energy density was uniform within the irradiated region whose geometry was a square, 320x320 μm. The laser system is synchronized with the underlying XYZ motion system such that a series of energy densities may be applied producing a spatial array on a single specimen. Each square region is an irradiated area of a single uniform energy density with 10 μm spacing. In addition, the effects of laser processing at elevated substrate temperatures have also been investigated through the use of a hot stage with controlled atmosphere. Substrate temperatures as high as 800° C are utilized while maintaining an inert atmosphere through argon flow in order to mitigate the effects of film oxidation. Additionally, it should be noted that attempts at crystallizing films at room temperature required the growth of a thin thermal oxide to enhance laser absorption. The details of this procedure can be found in Birnbaum et al [25].

Thin Film Melting Regimes

The process of thin film melting may be generally described by three distinct energy density regimes as developed by Im *et. al* [26]. These regimes are broken down by the extent to which the film has been melted through the thickness and are depicted schematically in Fig. 1. At low energy densities (relative to thermal, thermodynamic as well as specimen configuration), the laser energy absorbed by the film is not sufficient to completely melt the film through the thickness. This range of energy densities is termed the *partial melting* (PM) regime. In this case, for pre-crystallized films, resolidification proceeds via vertical epitaxial re-growth from the remaining un-melted seeds. Microstructures in this regime are characterized by grain sizes remain on the order of the film thickness.

At high energy densities, the energy provided by the laser is sufficient for complete through-thickness melting. This is the *complete melting* (CM) regime. For flood irradiated areas, solidification proceeds along two paths. The first is lateral epitaxial growth at the boundary of the irradiated area where adjacent solid seeds grow into the significantly undercooled melt resulting in long, high aspect ratio crystals. The other path is via nucleation and subsequent growth. This occurs away from the boundary of irradiation and results in planar, equiaxed grains. Microstructures in this regime thus consist of laterally grown grains at the boundary, and nucleated grains whose diameters can greatly exceed the film thickness.

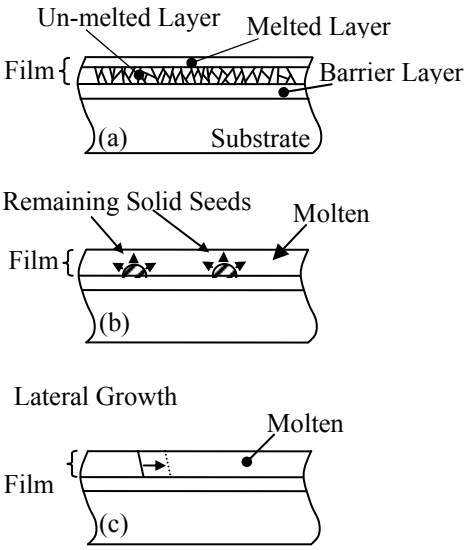

Fig. 1(a-c): Schematic representations of the (a) partial, (b) near complete and (c) complete melting regimes.

The final regime is the *near complete melting* (NCM) regime, and as the name suggests occurs over energy densities through which partial melting transitions to complete melting. Due to local inhomogeneities, for energy densities near the complete melt threshold (CMT), there are portions of the film that are completely melted and portions that are only partially melted. In this case solidification proceeds via two routes. The molten portions of the film go through nucleation and growth, while the near-complete melted seeds grow immediately upon reaching only slight undercoolings. The resulting grain size distribution is characterized by a bi-modal character with small grains having resulted from nucleation and growth, and large grains stemming from the remaining solid seeds that had added time for growth before being arrested by surrounding nucleants.

Results and Discussion

I. Resultant Phases

Laser irradiation of the films was initially performed over a range of energy densities with the substrate at room temperature. Employing the above mentioned method for optical absorption enhancement, the irradiated, initially amorphous regions of the film were successfully crystallized.

Figure 2 contains an x-ray diffraction (XRD) spectrum of a room temperature irradiated specimen, confirming the presence of crystalline material. As will be discussed later, it was also determined that the film had undergone complete melting, and thus nucleation and growth in order to solidify. The amorphous spectrum is included for reference. The presence of a single peak implies a strong normal texture suggesting the film had undergone heterogeneous nucleation at the film-barrier layer interface.

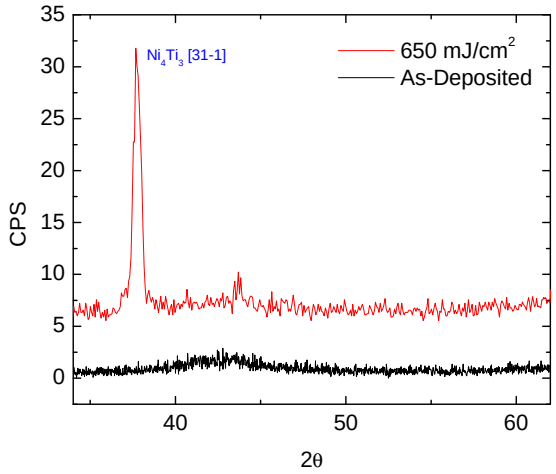

Figure 2: X-ray diffraction spectra for the as-deposited amorphous spectrum and the room temperature, laser treated specimen (completely melted) confirming crystallization as well as heterogeneous nucleation. Additionally, it is seen that a metastable Ni_4 Ti_3 phase results due to the exceedingly high quench rate.

Although crystallization was confirmed, after close scrutiny it was determined that the peak location for the crystallized film could not be indexed to either the martensite or austenite phase, and thus would not result in the desired shape memory response. Attempts to perform elevated temperature XRD also did not result in the emergence of any detectable austenitic peaks. The peak may be indexed to the metastable Ni_4Ti_3, [3-11] orientation. This is very likely due to the exceedingly high quench rate resulting from the pulsed laser process, which, particularly for concentrated alloys can be expected to result in the formation of metastable phases.

Upon discovering that laser processing at room temperature did not result in viable shape memory material, it was determined that processing at elevated substrate temperatures, that is pre-heating the specimen prior to and during laser irradiation would significantly reduce the quench rate, and thus have added potential for resulting in the desired phase(s). It should be noted however, that the preheating of the substrate actually results in solid phase crystallization (SPC) of the film *prior* to irradiation, and thus the crystallization process may no longer be seen as amorphous to crystal, but

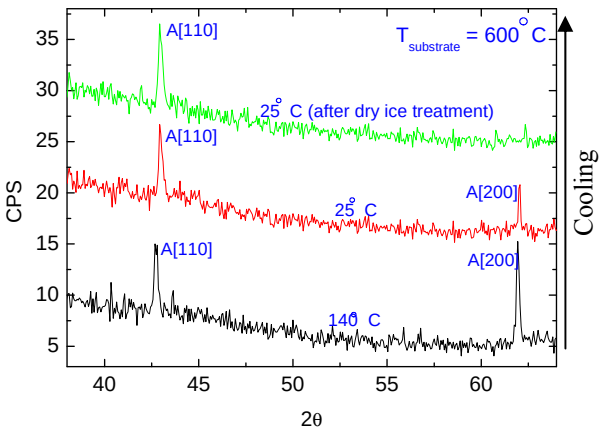

Figure 3: X-ray diffraction spectra depicting the thermally induced phase transformation. Note that emergence of the Austenitic phase upon heating, and subsequent disappearance upon cooling. The persistence of the [110] austenitic peak suggests a phase mixture of austenite and martensite upon cooling back down to room temperature.

now SPC matrix to laser induced crystal. While this will impact the specimen treated at energy densities below the CMT, it may be seen as having no effect on nucleated crystals having resulted from laser processing within the CM regime as for both cases, the transformation proceeds from liquid.

Substrate temperatures ranging from room temperature to 800° C were analyzed. It was seen that substrate temperatures below 600° C resulted in the previously seen Ni_4Ti_3 obtained from room temperature processing. However, at 600° C and above, significant changes in both the microstructure as well as the phase resulted.

Figure 3 contains XRD spectra collected from specimen laser treated at 600° C. Upon heating the specimen to 140° C, both the [110] and [200] austenitic peaks are present. After allowing the film to cool back down to room temperature, the [110] peak remains, but the [200] peak intensity decreases significantly. The specimen was then cooled with dry ice to -78° C and allowed to heat back up to room temperature. This resulted in a complete disappearance of the [200] peak, although the [110] peak persisted. Although no discernable martensitic peaks are detected, the appearance and subsequent disappearance of the [200] austenite upon cooling is direct evidence of the martensitic transformation. The incomplete disappearance of the [200] peak upon cooling suggests that room temperature lies within the hysteresis defined by the alloy's transformation start and finish temperatures.

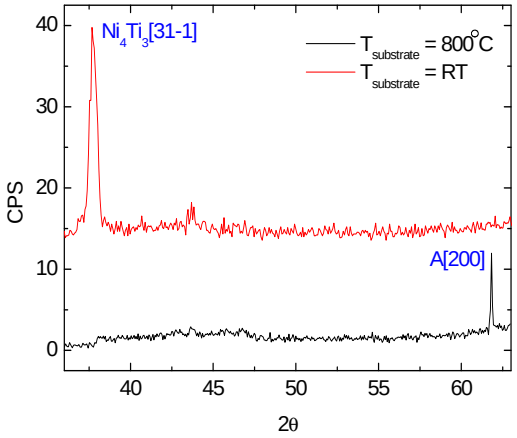

Figure 4: XRD spectra for room temperature and 800° C substrate temperature. Room temperature processing (ED=650 mJ/cm^2) results in metastable phase formation, while an elevated substrate temperature processing (ED=682 mJ/cm^2) results in the formation of Austenite. Note that both films were laser treated above their respective complete melt thresholds, and result in highly textured films implying heterogeneous nucleation.

Figure 4 reveals XRD spectra collected from specimen laser treated at room temperature and 800° C, both processed at energy densities above their respective CMT's. The change in peak location is evident after having processed at an elevated temperature. This peak is indexed as [200] austenite. In addition, it should be noted that only a single peak appears, again implying that the film solidified via heterogeneous nucleation and growth.

The apparent shift in martensitic phase transformation temperatures that results from processing at 600° C versus 800° C may be explained by a series of factors. Gil *et. al* [15] report an inversely proportional phase transformation temperature dependence on grain size. As the quench rate for the 800° C is lower than that of the 600° C processed specimen, this decreases the nucleation rate and thus allows added time and available volume for growth into the melt. Grain sizes from the 800° C film are in fact larger than their 600° C counterpart. Another factor that must be considered is the incorporation of oxygen into the film due to the pre-heating process. Although the hot stage specimen chamber was purged and continuously subjected to argon flow, oxidation was observed as a change in surface color from silver to gold. The color change was more severe at higher pre-heat temperatures due to increased oxidation rate. Otsuka and Wayman [28] report significant decreases in phase transformation temperatures as a function of oxygen content. This increased oxygen level in the film is consistent with

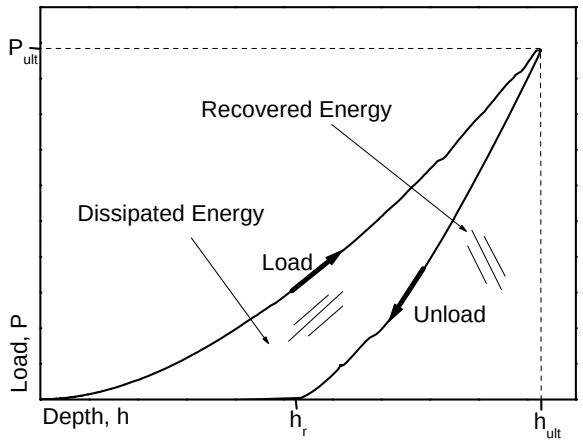

Figure 5: Schematic load curve for typical nanoindentation experiment. Note that the total energy input to the system is equal to the sum of the dissipated and recovered energy.

observing austenite at room temperature for the films treated at 800° C.

II. Mechanical and Shape Memory/Superelastic Response

II.1 Recoverable Energy

In addition to examining the melt and solidification process, a characterization of the load response via nanoindentation of laser treated specimen has also been performed over a range of energy densities and substrate temperatures.

In performing and analyzing nanoindentation experiments performed on shape memory materials, it is crucial that one takes into account their highly non-traditional constitutive response. Significant complications arise due to the presence of multiple possible deformation mechanisms being active upon loading *and* unloading. Upon loading, in addition to the elastic response, additional inelastic responses including plastic deformation via dislocation motion in the parent and/or martensitic phase, the stress induced martensitic phase transformation and/or martensitic twin reorientation [29]. Upon unloading, strain may also be recovered via elastic mechanisms in both the parent and martensite phases as well as the reverse stress induced martensite to austenite phase transformation. At sufficiently large indentation depths, further complexity appears due to contributions in the load response from the barrier layer/substrate. However, Fischer-Cripps [30] states that it is common practice to use ultimate indentation depths on the order of 10% of the film thickness in order to state with confidence that the response is film-dominated.

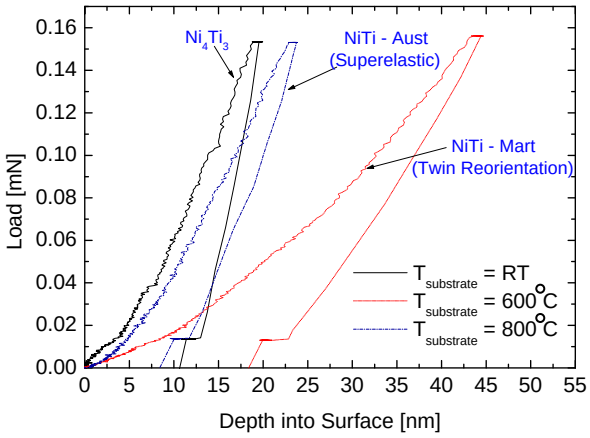

Figure 6: Load curve comparisons between specimens processed at room temperature (ED=650 mJ/cm^2), 600° C (ED=643 mJ/cm^2) and 800° C (ED=682 mJ/cm^2). Note that all specimens presented here were laser treated with energy densities above their respective CMT's.

In order to treat the added complexities introduced by the material, several authors [31, 32] have chosen to use the recoverable energy upon unloading as a metric for comparison. The recoverable energy upon unloading includes both elastic contributions from the parent as well as stress induced martensitic phases and the superelastic response from the reverse transformation. Using Fig. 5 as reference, it is seen that the total energy input to the system upon loading is:

$$W_{tot} = \int_0^{h_{ult}} P dh \qquad (1)$$

and the energy recovered upon unloading, the area under the unloading portion of the film, is calculated as:

$$W_{rec} = \int_{h_{ult}}^{h_{res}} P dh \qquad (2)$$

A recoverable energy ratio, η, may then be defined as the ratio of recovered to total input energy:

$$\eta = \frac{W_{rec}}{W_{tot}} \qquad (3)$$

Figure 6 shows the load response curves for specimens processed at room temperature, 600° C and 800° C. They are presented such that they all have comparable ultimate indentation loads, though significant differences in behavior are seen. It is seen that all three differ significantly in ultimate depth, unloading slope and residual depth. Within the context of the XRD spectra presented earlier, several observations can be made. It was shown earlier that the films processed at 600° C and 800° C are martensitic and

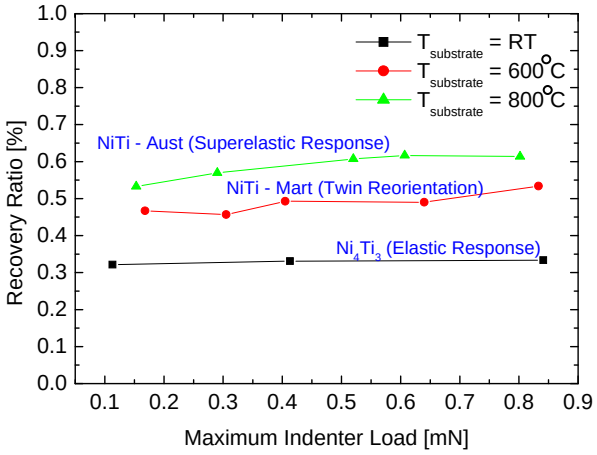

Figure 7: Energy recovery ratio as a function of maximum indenter load for films laser processed at room temperature (ED=650 mJ/cm^2), 600° C (ED=643 mJ/cm^2) and 800° C (ED=682 mJ/cm^2). It is seen here that the film processed at 800° C recovers significantly more energy upon unloading due to its superelastic response. Note that all specimens presented here were laser treated with energy densities above their respective CMT's.

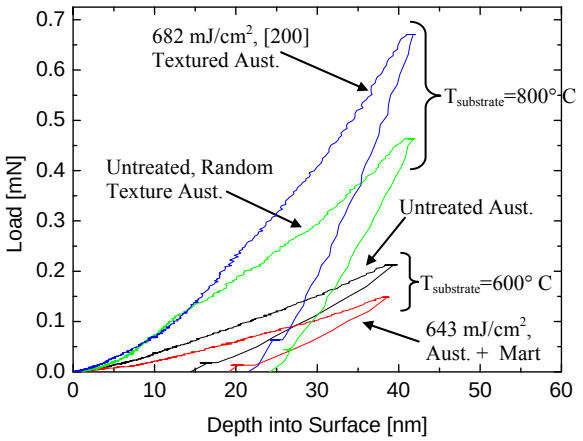

Figure 8: Load responses of laser treated and untreated films for elevated substrate temperatures of 600° C and 800° C. Note the increased slope, as well as increased depth recovery for the laser treated, [200] textured film treated at 800° C.

austenitic at room temperature respectively. This is manifested as a significantly larger residual depth for the martensitic film due to inelastic martensitic twin reorientation, as opposed to the enhanced depth recovery due to superelasticity for the austenitic film. The relative ease with which twin reorientation is also noted and manifested by the significantly increased ultimate depth required to generate a comparable indenter load.

Figure 7 is a plot of the recoverable energy ratio as a function of ultimate applied indenter load for specimen laser treated at room temperature, 600° C and 800° C. All three specimens have been treated with energy densities above their corresponding CMT's. It is seen that the specimens treated at 600° C and 800° C recover significantly more energy upon unloading than that processed at room temperature. It has already been confirmed via XRD that the specimen processed at 800° C is austenitic at room temperature and thus exhibits a superelastic response, explaining the ability to recover the most energy upon unloading. This enhanced energy recovery is also consistent with Gall et. al.'s [29] examination which showed that the [200] austenite surface normal orientation is particularly effective in recovering energy upon unloading. It was shown above via XRD that the film processed at 800° C does indeed have a strong [200] normal texture due to having been heterogeneously nucleated. In addition, the solid-phase crystallized, untreated film only shows a 42% energy recovery. Thus manipulating the film's microstructure to result in a strong [200] normal texture has significantly increased the ability to recover energy and holds compelling implications for wear resistance applications.

XRD also revealed that the specimen processed at 600° C is a phase mixture of austenite and martensite upon cooling from the fully austenitic state. This decrease in recoverable energy relative to that processed at 800° C is explained by a corresponding increase in energy dissipated through martensitic twin reorientation while loading. A slight increase in the ratio is seen as the maximum load increases for the specimens processed at 600° C and 800° C. This could be due to an increase in elastic contribution from the underlying barrier layer. However, since the room temperature treated specimen does not show a corresponding increase at comparable load, it is also possibly due to increased recovery from the reverse transformation relative to that dissipated by plastic flow.

II.2 Effective Film Modulus

In addition to examining the recoverable energy ratio, the elastic response was also characterized via the more traditional elastic unloading analysis. However, it is stressed that the elastic moduli presented here represent an *effective* film modulus. This effective modulus, as explained above is the manifestation of several deformation mechanisms operating simultaneously upon unloading.

From the Hertz derivation, it is seen that the *reduced* modulus which accounts for the properties of both the film and indenter is given by:

$$\frac{1}{E_r} = \frac{(1-\nu_f^2)}{E_f} + \frac{(1-\nu_i^2)}{E_i} \qquad (4)$$

where ν_f and E_f and ν_i and E_i are the Poisson's ratio and Young's Modulus of the film and indenter respectively. E_r may be obtained from the experimentally obtained load curve by utilizing the expression derived by Oliver and Pharr [33] for conical indenters: $E_r = \frac{S}{2\beta}\sqrt{\frac{\pi}{A}}$ (5) where $S = \frac{dP}{dh}$ is the initial slope of the unloading curve, β is a geometric factor, in this case equaling 1.034 (Berkovich indenter) and A is the projected area of contact at the ultimate measured depth. Using the known properties of the indenter, $E_i = 1141$ GPa and $\nu_i = 0.07$, and assuming a Poisson's ratio of 0.35 for the film, it is then possible to calculate the effective film modulus from equations 4 and 5.

Load curves at comparable ultimate indentation depths for the 600° C and 800° C substrate temperature conditions, unprocessed and laser treated are presented in Fig. 8. For the 600° C case, it is seen that the untreated austenitic film results in lower residual depths due to the superelastic strain recovery, while the laser treated martensitic film requires less indenter load to achieve a comparable indentation depth due to the relative ease with which martensitic twin variants may be reoriented. The 800° C case differs in that both the untreated and laser processed film are both austenitic. However, it was shown in the discussion above that due to having been heterogeneously nucleated, the laser processed film results in a strong [200] texture. This is manifested as an increase in the unloading slope of the curve, as well as enhanced depth and energy recovery due to the anisotropy of the response.

The effective elastic moduli calculated from the load responses are summarized in Fig. 9. For clarification, the "untreated" properties presented in the figure are effective moduli of films that have been preheated, and thus solid phase crystallized, but have not been laser treated. All of the laser treated properties presented in Fig. 9 are from regions that have undergone complete melting, and therefore nucleation and growth. The untreated values of effective modulus for the 600° C, 700° C and 800° C pre-heated and solid phase crystallized films are those of randomly textured austenite as confirmed by XRD (not shown).

Substrate Temp.	Process Condition	Effective Modulus
RT	Amorphous, As-Deposited	224 ± 34 [Gpa]
	Laser Treated*	260 ± 34 [Gpa]
600° C	Untreated	61 ± 6 [Gpa]
	Laser Treated*	44 ±1 [Gpa]
700° C	Untreated	106 ± 7 [Gpa]
	Laser Treated*	112 ± 6 [Gpa]
800° C	Untreated	136 ± 22 [Gpa]
	Laser Treated*	171 ± 19 [Gpa]

Figure 9: Effective film modulus for films laser processed at room temperature (ED=650 mJ/cm^2), 600° C (ED=643 mJ/cm^2) and 800° C (ED=682 mJ/cm^2). *Laser treated specimen presented here have undergone complete melting, and thus nucleation and growth in order to solidify.

However, the untreated effective modulus values increase as a function of pre-heat temperature. This is most likely due to increases in surface oxidation with increased pre-heat temperatures. Increased oxidation rates result in thicker surface oxides which result in an enhanced contribution to the load response, particularly at shallow indentation depths. Thus comparisons should be made between treatments at comparable pre-heat temperatures. The 700° C and 800° C both show qualitatively similar results in that the laser treated films result in increased effective modulus. This is explained by the anisotropic dependence on both elastic modulus and transformation stress. The initial solid phase crystallized films have a relatively random texture, whereas the films that have been treated above their CMT's result in strong normal textures due to their having solidified via heterogeneous nucleation. The film processed at 600° C actually shows a substantial decrease in effective modulus. This is due to a shift in phase transformation temperature resulting in an alloy that is martensitic at room temperature in contrast to the films treated at 700° C and 800° C.

III. Microstructure

Substrate temperatures ranging from room temperature to 800° C were analyzed. A full analysis and characterization of room temperature processed films was performed by Birnbaum et al. [25].It should be noted that films processed at temperatures below 600° C result in similar microstructures, as well as microstructural trends as a function of incident energy density. However, at 600° C and above, significant changes in both the microstructure as well as the phase resulted. Figures 10(a-f) are micrographs obtained via scanning electron microscopy (SEM) for specimens processed at 800° C. Figures 10(a, c, e) and 10(b, d, f)

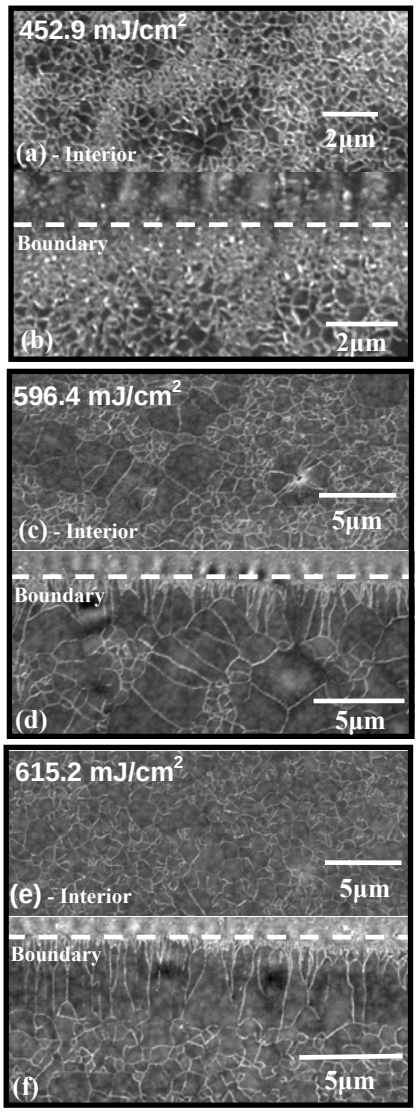

Figure 10: Scanning Electron Micrographs, $T_{substrate}$=800° C: (a,b) Interior and boundary regions respectively. Partially melted film characterized by small grain size limited to film thickness, ED=452.91 mJ/cm^2. (c,d) Interior and boundary regions respectively. Near complete melting regime characterized by bi-modal grain size distribution, ED=596.4 mJ/cm^2. (e,f) Interior and boundary regions respectively. Completely melted film characterized by the presence of large aspect ratio, well defined lateral growth, ED=615.2 mJ/cm^2.

are obtained from laser treated areas away from and at the boundary of irradiation respectively. The microstructures presented in these figures have also been quantitatively analyzed, and both grain size and representative grain size distributions as a function of %CMT are found in Fig. 11. The three sets of micrographs are also representative of the

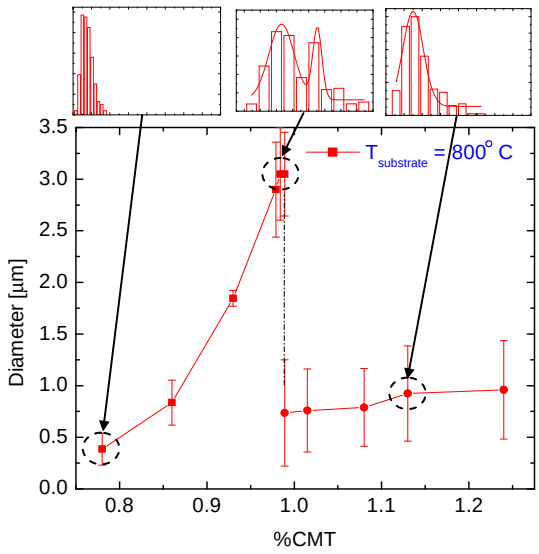

Figure 11: Average grain size as a function of % Complete Melt Threshold (CMT). Note the evolution of grain size distribution as the energy density transitions through the partial, near complete and complete melting regimes.

microstructures resulting from processing at energy densities within the three thin film melting regimes discussed earlier. Although the micrographs presented here are limited to the 800° C substrate case, the 600° C and 700° C microstructures have been analyzed, and follow the same phenomenological trend, i.e. PM, NCM and CM transitions. However, it should be noted that, as may be expected, there are differences in actual grain sizes and shifts in CMT due to the variation in substrate temperature.

Figures 10(a, b) are micrographs representative of the resulting microstructures processed at energy densities within the PM regime. This is seen by the reduced grain size, i.e. grain sizes restricted by film thickness, as well as the fact that no lateral growth is present at the irradiated boundary. The detail provided in Fig. 16 at 78% CMT reveals an average grain size and distribution. Figures 10(c, d) are micrographs obtained from specimen laser treated at 99% of the CMT. A significant increase in average grain size, as well as a transition to a bi-modal grain size distribution is in both the micrographs and detail in Fig. 11. In addition, the presence of some lateral growth is seen at the boundary as may be expected in the NCM regime. Finally, Figs. 10(e, f) are micrographs from specimen laser treated at 102% of CMT. Average grain size diminishes substantially, and the character of the grain size distribution changes to a single mode, log-normal distribution (see detail in Fig. 11). Most importantly however, is the presence of well defined lateral growth at the boundary which is direct evidence of film having

undergone complete melting, and therefore nucleation and growth.

Conclusion

It has been shown that laser processing of films at elevated temperatures through the use of pre-heated substrates has a dramatic influence on their microstructure, phase, mechanical and shape memory responses. Furthermore, it has been demonstrated that laser crystallization of pre-crystallized randomly textured austenitic films results in strong normal textures that are favorable with respect to energy recovery having strong implications for wear resistance applications. In terms of application, the requirement for pre-heated substrates does present some drawbacks, such as oxidation and potential incompatibility with temperature sensitive substrates. It also prevents the user from crystallizing within an amorphous matrix, as the pre-heat results in solid phase crystallization. However, it has also been shown that laser processing at room temperature results in the production of non-shape memory phases. Thus a shape memory subtractive process may be implemented on crystalline films in order to spatially control the presence of shape memory responses. Additionally, techniques such as combining laser irradiation while utilizing a focused flash lamp to heat the film over microsecond time scales can enable the reduced quench rate required for desired phase formation, while maintaining the film's amorphous as-deposited state.

References

[1] Simidzu, H. , Katayama, S. & Mastunawa, A. (1991), "Laser Rapid Solidification Microstructure of Single Crystal Aluminum Alloys", Proceedings of the Laser Materials Processing - ICALEO '90, 492-501.

[2] Lin, C.J. & Spaepen, F. (1986), "Nickel-NiobiumAlloys Obtained by Picosecond Pulsed Laser Quenching", *Acta Metallurgica*, v 34, n 7, p 1367-1375.

[3] Sposili, R., Crowder, M. & Im, J.S. (1997) "Single-Crystal Si Films Via a Low-Substrate-Temperature Excimer-Laser Crystallization Method", *MRS - Proceedings*, v 452, *Advances in Microcrystalline and Nanocrystalline Semiconductors*, p 953-958.

[4] J.P. Leonard, "Nucleation Rate in the Si-SiO_2 Thin Film System", Doctoral Thesis, Columbia University, 2000.

[5] Lin, C.-J., Spaepen, F. & Turnbull, D. (1983), "Picosecond Pulsed Laser-Induced Melting and Glass Formation in Metals", *Journal of Non-Crystalline Solids*, v 61-62, n pt 2, Jan, p 767-772.

[6] Lin, C.-J. & Spaepen, F. (1984), "Metallic Glasses and Metastable Crystalline Phases Produced by Picosecond Pulsed Laser Quenching", *Materials Research Society Symposia Proceedings*, v 28, p 75-80.

[7] Spaepen, F. (1986), "Thermodynamics and Kinetics of Metallic Alloy Formation by Picosecond Pulsed Laser Irradiation", *High Temperature Materials and Processes*, v 7, n 2-3, p 91-100.

[8] Hau-Riege, C.S., Hau-Riege, S.P. & Thompson, C.V. (2001), "Simulation of Microstructural Evolution Induced by Scanned Laser Annealing of Metallic Interconnects", *Journal of Electronic Materials*, v 30, n1,p.11-16.

[9] Li, D.Y., (1998), "A new type of wear-resistant material: pseudo-elastic TiNi alloy", *Wear,* 221 p.116–123.

[10] Gialanella, S., Ischia, G. and Straffelini, G., (2008), "Phase composition and wear behavior of NiTi alloys", *Journal of Material Science,* 43, 1701–1710.

[11] Tan, L., Crone, W.C. and Sridharan, K., (2002), "Fretting Wear Study of Surface Modified Ni-Ti Shape Memory Alloy", *Journal of Material Science:Materials in Medecine,* 13, 501-508.

[12] Ishida, A. & Sato, M. (2003), "Thickness effect on shape memory behavior of Ti-50.0at.%Ni thin film", *Acta Materialia,* 51, 5571–5578.

[13] Ishida, A., Takei, A., Sato, M. & Miyazaki, S. (1995), "Shape Memory Behavior of Ti-Ni Thin Films Annealed at Various Temperatures", *Materials Research Society Symposia Proceedings*, v 360, 381-386.

[14] Ishida, A., Takei, A., Sato, M. & Miyazaki, S. (1996), "Stress-Strain Curves of Sputtered Thin Films of Ti-Ni", *Thin Film Solids,* 281-282, 337-339.

[15] Gil, F.J., Manero, J.M. & Planell, J.A. (1995), "Effect of Grain Size on the Martensitic Transformation in NiTi Alloy", *Journal of Material Science*, 30, 2526-2530.

[16] Lee, H.-J., Ni, H., Wu, D. T., & Ramirez, A.G. (2005), "Grain size estimations from the direct measurement of nucleation and growth" *Applied Physics Letters* 87, 124102.

[17] Lee, H.-J. & Ramirez, A.G. (2004), "Crystallization and Phase Transformations in Amorphous NiTi Thin Films for Microelectromechanical Systems", *Applied Physics Letters*, Vol. 85, No. 7, 1146-1148.

[18] Makino, E., Mitsuya, T. & Shibata, T. (2000), "Dynamic actuation properties of TiNi shape memory diaphragm", *Sensors and Actuators* 79, 128–135.

[19] Wibowo, E., Kwok, C. Y. & Lovell, N. H. (2004) "Two-way Actuation of Bi-layer Cantilever of Nickel Titanium and Silicon Nitride Thin Films by Shape Memory Effect and Stress Relaxation", Device and

Process Technologies for MEMS, Microelectronics, and Photonics III, Proceedings of SPIE Vol. 5276.

[20] Selden, B., Cho, K. & Asada, H. (2006), "Segmented shape memory alloy actuators using hysteresis loop control", *Smart Materials and Structures*, 15, 642–652.

[21] Makino, E., Mitsuya, T. & Shibata, T. (2000),"Micromachining of TiNi Shape Memory Thin Film 10 for Fabrication of Micropump", *Sensors and Actuators*, 79, 251–259.

[22] Wang, X., Bellouard, Y. & Vlassak, J.J. (2005), "Laser Annealing of Amorphous NiTi Shape Memory Alloy Thin Films to Locally Induce Shape Memory Properties", *Acta Materialia*, 53, 4955–4961.

[23] Bellouard, Y., Lehnert, T., Bidaux, J.-E., Sidler, T., Clavel, R. & Gotthardt, R. (1999), "Local annealing of complex mechanical devices: a new approach for developing monolithic micro-devices", *Materials Science and Engineering A*, 795–798.

[24] He, Q., Hong, M.H., Huang, W. M., Chong, T. C., Fu, Y. Q. & Du, H. J. (2004), "CO2 Laser Annealing of Sputtering Deposited NiTi Shape Memory Thin Films", *Journal of Micromechanics and Microengineering*, 14, 950–956.

[25] Birnbaum, A.J., Chung, U.J., Hung, X., Ramirex, A.G., Polvino, S. and Yao, Y.L., (2007), "Melt-Mediated Laser Crystallization of Thin Film NiTi Shape Memory Alloys", *Proceedings of ICALEO-Laser Materials Processing, p. 98-107.*

[26] Im, J.S., Kim, H.J. and Thompson, M.O., (1993), "Phase Transformation Mechanisms Involved in Excimer Laser Crystallization of Amorphous Silicon Films", *Applied Physics Letters*, 63, 1969-1971.

[28] Otsuka, K. and Wayman, C.M., (1998), "Shape Memory Materials", Cambridge University Press, Cambridge, U.K.

[29] Gall, K. Juntunen, K., Maier, H.J., Sehitoglu, H. and Chumlyakov, Y.I., (2001), "Instrumented Micro-Indentation of NiTi Shape Memory Alloys," Acta Materialia, 49, 3205–3217.

[30] Fischer-Cripps, A.C., (2004), "Nanoindentation", 2nd Ed., Springer-Verlag, New York, N.Y.

[31] Liu, R. and Li, D.Y., (1999), "Indentation Behavior of Pseudoelastic TiNi Alloy," *Scripta Materialia*, Vol. 41, No. 7, 691–696.

[32] Ni, W.., Cheng, Y., Grummon, D.S., (2004), "Microscopic Shape Memory and Superelastic Effects Under Complex Loading Conditions," *Surface and Coatings Technology,* 177 –178, 512–517.

[33] Oliver, W.C. and Pharr, G.M., (1992), "An Improved Technique for Determining Hardness and Elastic Modulus Using Load and Displacement Sensing Indentation Experiments", *Journal of materials research*, vol. 7, iss. 6, 1564 -1580.

Meet the Authors

Andrew J. Birnbaum received his B.S and M.S. from Carnegie Mellon University. He is currently a doctoral student at the Manufacturing Research Laboratory at Columbia University.

Dr. Xu Huang is a Postdoctoral Associate in Department of Mechanical Engineering at Yale University. His research interests are in shape memory alloys and electronic packaging. He received his doctorate degree from Nanyang Technological University, Singapore, master's degree from University of Science and Technology Beijing, and bachelor's degree from Southern Institute of Metallurgy, P.R. China, all in materials science and engineering.

Dr. Ainissa G. Ramirez is an Associate Professor of Mechanical Engineering at Yale University. Prior to her appointment at Yale, she was a member of technical staff at Bell Laboratories, Lucent Technologies in Murray Hill, NJ. Her research interests are in thin film shape memory alloys and universal solders. She received her doctorate and master's degrees from Stanford University, and bachelor's degree from Brown University, all in materials science and engineering.

Dr. Ui-Jin Chung received his B.S., M.S. and PhD from Seoul National University in Material Science and Engineering. He previously worked as a senior engineer at Samsung Electronics and is currently an associate research scientist in the laser crystallization lab at the Applied Physics and Applied Math Department, Columbia University.

Dr. James S. Im is currently a materials science professor in the Applied Physics Dept. at Columbia University. He received his B.S. from Cornell, and PhD from MIT.

Dr. Y. Lawrence Yao is currently department chair of Columbia University's Mechanical Engineering Department and director of the Manufacturing Research Laboratory. He received his Ph.D. from the University of Wisconsin-Madison in 1988. He also serves on the Board of Directors of LIA.